

# Characterizing the zenithal night sky brightness in large territories: How many samples per square kilometer are needed?

Salvador Bará <sup>1,\*</sup>

<sup>1</sup>*Facultade de Óptica e Optometría, Universidade de Santiago de Compostela, 15782 Santiago de Compostela, Galicia, Spain.*

\* [salva.bara@usc.es](mailto:salva.bara@usc.es)

## Abstract

A recurring question arises when trying to characterize, by means of measurements or theoretical calculations, the zenithal night sky brightness throughout a large territory: how many samples per square kilometer are needed? The optimum sampling distance should allow to reconstruct with sufficient accuracy the continuous zenithal brightness map across the whole region, whilst at the same time avoiding an unnecessary and redundant oversampling. This paper attempts to provide some tentative answers to this issue, using two complementary tools: the luminance structure function and the Nyquist-Shannon spatial sampling theorem. The analysis of several regions of the world, based on the data of the *New world atlas of artificial night sky brightness* (Falchi et al 2016, Sci. Adv. 2, e1600377) suggests that, as a rule of thumb, about one measurement per square kilometer could be sufficient for determining the zenithal night sky brightness of artificial origin at any point of a region to within  $\pm 0.1 \text{ mag/arcsec}^2$  (in the root-mean-square sense) of its true value in the Johnson-Cousins V band. The exact reconstruction of the zenithal night sky brightness maps from samples taken at the Nyquist rate seems to be considerably more demanding.

Keywords: Artificial light at night, light pollution, radiometry, photometry

## 1. Introduction

The night sky brightness in vast regions of the world is significantly higher than its expected natural value [1-5], due to the atmospheric scattering of visible photons emitted by artificial light sources. This is one of the most conspicuous manifestations of light pollution, a generic term that encompasses the unwanted consequences of the present way of using artificial light. Significant efforts have been devoted in the last years to model and quantify this phenomenon [6-16], as well as to evaluate its effects on the environment [17-23].

Several radiometric magnitudes can be used to characterize the night sky brightness (NSB), and to evaluate its departure from the expected natural conditions at any given site. The most comprehensive description is provided by the spectral radiance (in  $\text{Wm}^{-2}\text{sr}^{-1}\text{nm}^{-1}$ ), specified for all directions of the sky hemisphere above the observer and for all wavelengths of the optical spectrum. The measurement of the spectral radiance, however, requires using relatively complex and expensive equipment (e.g. sequential spectrometers or all-sky hyperspectral cameras), and this has precluded its generalized use in field conditions. A technically simpler but still highly useful approach is all-sky imaging in the Johnson-Cousins B, V and R bands [24-27], or conventional DSLR RGB imagery [28-29]. The all-sky photopic brightness evaluated in the  $V(\lambda)$  band or, as an approximation, in the Johnson-Cousins V, allows to calculate a relevant set of visual parameters at the observer's site [30].

The zenithal NSB, despite having a considerably smaller information content than the all-sky distributions described above, is widely used nowadays to characterize the anthropogenic disruption of the natural night. This is partly due to the widespread availability of low-cost detectors that enable its straightforward measurement, by professional and citizen scientists alike, in many countries of the world [4-5, 31-36]. The zenithal NSB at any observing site is not a fixed number, but a random variable

that depends on the changing state of the atmosphere (most notably on the aerosol concentration profile and on the presence and type of clouds), on the deterministic evolution of the light emissions from artificial sources located in a region that may be hundreds of km wide, and on the natural sources located above the observer (celestial objects in the zenithal region of the sky, and natural airglow). Under a layered atmosphere the zenithal NSB varies from site to site due to the change in the relative positions of the artificial sources with respect to the observer, as well as to the particular distribution of obstacles that may block the atmospheric light propagation along certain paths. The zenithal NSB at neighbouring locations, however, tends to be partially correlated, since the scattering at any elementary volume of the air column above each observer involves multiple superposition integrals of the radiances emitted by a shared set of artificial sources. The question arises, then, of which is the maximum permissible distance between adjacent measurements in a given territory, in order to ensure that after a suitable mathematical processing a reasonably accurate reconstruction of the true zenithal night sky brightness can be achieved for all of its points.

Some tentative answers to this issue are explored in this paper, based on the analysis of the luminance structure function and on the spatial version of the Nyquist-Shannon sampling theorem, whose definition and properties are described in Section 2. To get some insight about the expected order of magnitude of the optimal sampling distance, both methods are applied in Section 3 to the zenithal NSB distributions in several regions of the world, whose artificial component has been estimated by Falchi et al. in the *The new world atlas of artificial night sky brightness* [2-3], henceforth referred to as the NWA. The analysis performed for the artificial component of the zenithal NSB in Section 3.1. is extended to the total one in Section 3.2., and the differences and similarities between both cases are pointed out. As a result, some practical consequences can be extracted regarding the optimum sampling distance under a variety of situations. The significance and limitations of this study are addressed in Section 4, and Conclusions are drawn in Section 5.

## 2. Methods

The methods described in this section can be equally applied to the artificial component of the night sky brightness or to the total one, including the contribution of natural sources like celestial bodies and atmospheric airglow. Separate quantitative results for each case will be presented in Section 3.

### 2.1. The zenithal sky brightness spatial structure function

Let  $L(\mathbf{r})$  be the zenithal night sky brightness recorded by an observer located at the point  $\mathbf{r}$  in a given geographical region. "Sky brightness" is a short-hand term for the integral over wavelengths of the spectral radiance at the entrance of the detector, weighted by the spectral filter function of the photometric band in which the observations are carried out, e.g. the Johnson-Cousins V [37], or the CIE scotopic  $V'(\lambda)$  or photopic  $V(\lambda)$  bands [38]. When the weighting function is the spectral efficacy of the human visual system for the appropriate level of luminance adaptation (photopic or scotopic), the resulting sky brightness can be expressed in SI luminance units of  $\text{cd}/\text{m}^2$ , equivalent to  $\text{lx}/\text{sr}$ . Otherwise, and according to the SI recommended practice, its value is given in weighted  $\text{Wm}^{-2}\text{sr}^{-1}$ , specifying the measurement band.

The night sky brightness has a wide dynamic range, and it is often conveniently expressed in the negative logarithmic scale of magnitudes per square arcsecond ( $\text{mag}/\text{arcsec}^2$ ). The weighted radiance  $L$  in the Johnson-Cousins V band and its value  $m$  in  $\text{mag}/\text{arcsec}^2$  are related by [5-6]:

$$L[\text{Wm}^{-2}\text{sr}^{-1}] = 158.1 \times 10^{(-0.4m)} \quad (1)$$

The associated SI luminance, in  $\text{cd}/\text{m}^2$ , is conventionally estimated as [4-6]

$$L[\text{cd}\cdot\text{m}^{-2}] = 10.8 \times 10^4 \times 10^{(-0.4m)}, \quad (2)$$

which results from the multiplication of Eq. (1) by the 683  $\text{lm}/\text{W}$  scale factor that accounts for the maximum luminous efficacy of the optical radiation for photopically

adapted eyes. Note, however, that Eq. (2) is only approximate, because the Johnson-Cousins V and the CIE photopic  $V(\lambda)$  bands are not strictly equivalent [39].

When moving from  $\mathbf{r}$  to a neighbouring place  $\mathbf{r}' = \mathbf{r} + \mathbf{d}$ , the zenithal sky brightness  $L(\mathbf{r})$  changes to  $L(\mathbf{r}')$ . The difference  $L(\mathbf{r} + \mathbf{d}) - L(\mathbf{r})$  generally depends on  $\mathbf{r}$  and  $\mathbf{d}$ , and shall be evaluated on a case by case basis. However, some insights about its expected behaviour can be obtained by computing the spatial average of its squared value over an extended area,  $S$ . The result is the *zenithal sky brightness spatial structure function*, defined in energy or luminance units as

$$D_L(\mathbf{d}) = \langle [L(\mathbf{r} + \mathbf{d}) - L(\mathbf{r})]^2 \rangle = \frac{1}{S} \iint_S [L(\mathbf{r} + \mathbf{d}) - L(\mathbf{r})]^2 d^2\mathbf{r}, \quad (3)$$

where  $d^2\mathbf{r} = dx dy$  is the surface element in  $S$  and the brackets denote spatial averaging. If the zenithal brightness data are available as an array of finite-sized spatial pixels, the integral in Eq. (3) becomes a finite sum. Note that Eq. (3) can equivalently be written as:

$$D_L(\mathbf{d}) = \langle [L(\mathbf{r} + \mathbf{d})]^2 \rangle + \langle [L(\mathbf{r})]^2 \rangle - 2\langle L(\mathbf{r} + \mathbf{d})L(\mathbf{r}) \rangle, \quad (4)$$

whose last term is the *zenithal sky brightness spatial correlation function*  $B_L(\mathbf{d}) = \langle L(\mathbf{r} + \mathbf{d})L(\mathbf{r}) \rangle$ . In the limit of very large averaging areas (i.e., those whose linear dimensions are very large compared with the modulus of  $\mathbf{d}$ ), we have  $\langle [L(\mathbf{r} + \mathbf{d})]^2 \rangle = \langle [L(\mathbf{r})]^2 \rangle = \sigma_L^2$ , where  $\sigma_L^2$  is the mean squared value of  $L(\mathbf{r})$  in  $S$ . Consequently, for large  $S$ , the spatial structure and correlation functions are related by

$$D_L(\mathbf{d}) = 2\sigma_L^2 - 2B_L(\mathbf{d}). \quad (5)$$

The spatial structure function can also be defined for the zenithal night sky brightness expressed in mag/arcsec<sup>2</sup> units,  $m(\mathbf{r})$ , as

$$D_m(\mathbf{d}) = \langle [m(\mathbf{r} + \mathbf{d}) - m(\mathbf{r})]^2 \rangle. \quad (6)$$

Equations similar to Eqs. (4)-(5) immediately follow, after substituting of  $m$  for  $L$ .

The expected change of the zenithal sky brightness as the observer moves from its initial observing place  $\mathbf{r}$  to a new position  $\mathbf{r}' = \mathbf{r} + \mathbf{d}$  can be estimated (in the rms

sense) by the square roots of  $D_L(\mathbf{d})$  and  $D_m(\mathbf{d})$ . Both functions have zero value for  $\mathbf{d} = \mathbf{0}$ , and tend to increase, albeit not necessarily in a monotonic way, for increasing values of the distance  $d = |\mathbf{d}|$ . Note that, generally, the change in brightness does not only depend on  $d$ , but also on the displacement direction  $\hat{\mathbf{d}} = \mathbf{d}/|\mathbf{d}|$ , where  $\hat{\mathbf{d}}$  stands for "unit vector". The function  $\sqrt{D_L(\mathbf{d})}$  provides the expected rms brightness change in absolute, energy-related, light units  $\text{cd/m}^2$  or weighted  $\text{Wm}^{-2}\text{sr}^{-1}$ .  $\sqrt{D_m(\mathbf{d})}$ , in turn, gives us the relative change in  $\text{mag/arcsec}^2$ , that is, as  $-2.5$  times the logarithm of the ratio of the final to the initial brightnesses.

Whether to use one or another function for estimating the maximum sampling distance depends on the way of specifying the desired reconstruction accuracy goals.  $\sqrt{D_L(\mathbf{d})}$  is the function of choice when the tolerance threshold  $\gamma$  (the maximum allowed rms difference between the measured and true luminances at the intermediate area between sampling points) is expressed in  $\text{cd/m}^2$  or  $\text{Wm}^{-2}\text{sr}^{-1}$ .  $\sqrt{D_m(\mathbf{d})}$  shall be used, in turn, if the tolerance is expressed as a maximum allowed relative error, e.g.  $\pm 0.1 \text{ mag/arcsec}^2$ . Once specified this goal, the optimum sampling distance  $d_s$  can be chosen as the value of  $d$  at which the square root of the corresponding structure function attains the established threshold. Note that  $d_s$  will generally depend on the displacement direction  $\hat{\mathbf{d}}$ . A conservative, uniform, and relatively small value of  $d_s$  may be adopted for all displacement directions, or a different value  $d_s(\hat{\mathbf{d}})$  may be used for each direction if some information about the spatial distribution of the zenithal night sky brightness, or the artificial sources that produce it, is a priori available.

### ***B. The spatial spectrum of the zenithal sky brightness and the Nyquist-Shannon sampling theorem***

The classical version of the Nyquist-Shannon sampling theorem [40] states that a spectrally band-limited time signal  $f(t)$  can be *exactly* reconstructed from a discrete set of samples,  $f(t_n)$ , taken at periodic times separated by a fixed interval  $\tau_s$  (that is, at  $t_n = t_o + n\tau_s$ , with arbitrary  $t_o$ , and  $n$  integer), as far as  $\tau_s \leq 1/(2\nu_s)$ , where  $\nu_s$  is the

maximum temporal frequency (Hz) present in the signal spectrum. The limiting time interval  $\tau_s = 1/(2\nu_s)$  is known as the Nyquist sampling rate. The reconstruction of the original signal from this discrete set of samples is carried out by a low-pass filtering of the spectrum of the sampled signal, followed by an inverse Fourier transform for going back to the time domain. The net result of these operations is equivalent to interpolating the signal between samples by using a set of scaled  $\text{sinc}_n(t) = \sin[2\pi\nu_s(t-t_n)]/[2\pi\nu_s(t-t_n)]$  functions centered at the sampling points [40]. The most interesting feature of this theorem is that this interpolation does not merely approximate the values of the function between measurement points, but provides an *exact* reconstruction of  $f(t)$  (noise propagation aside) for *all values* of  $t$ .

The Nyquist-Shannon theorem in the one-dimensional time domain can be easily extended to spaces of higher dimension. A classical two-dimensional formulation has been developed fifty years ago for applications in the field of coherent optics [40-41]. Adapted to our present issue, let us define the two-dimensional spectrum  $\Lambda(\mathbf{v})$  of  $L(\mathbf{r})$  as the Fourier transform:

$$\Lambda(\mathbf{v}) = \iint_{\infty} L(\mathbf{r}) \exp(-i2\pi\mathbf{v} \cdot \mathbf{r}) d^2\mathbf{r}, \quad (7)$$

where  $\mathbf{v} = (v_x, v_y)$  is a vector whose components (units  $\text{m}^{-1}$ ) play a role analog to the time frequency, but now along the two orthogonal dimensions of the inverse space domain. The Nyquist-Shannon theorem states that if the function  $L(\mathbf{r})$  is band-limited, that is, if its spectrum  $\Lambda(\mathbf{v})$  becomes zero for spatial frequencies  $v_x > v_{x\text{max}}$  and  $v_y > v_{y\text{max}}$ , then  $L(\mathbf{r})$  can be exactly reconstructed at all points of its definition domain from a discrete set of samples  $L(\mathbf{r}_{pq})$  taken at a rectangular grid of points  $\mathbf{r}_{pq} = (x_o + pd_{sx}, y_o + qd_{sy})$ , with arbitrary  $(x_o, y_o)$ ,  $p$  and  $q$  integers, as far as  $(d_{sx}, d_{sy}) \leq (1/(2v_{x\text{max}}), 1/(2v_{y\text{max}}))$ . The latter condition states that the spatial sampling period along each orthogonal direction shall be smaller than half the inverse of the maximum spatial frequency present in the signal spectrum along that direction. The exact reconstruction of the original function  $L(\mathbf{r})$  is carried out, analogously to the one-dimensional time case, by a low pass filtering of the spectrum of  $L(\mathbf{r}_{pq})$  in the

spatial frequency domain, followed by an inverse two-dimensional Fourier transform for going back to the space domain. This is equivalent to using a set of scaled two-dimensional sinc functions, centered at the sampling points, to exactly interpolate the values of  $L(\mathbf{r})$  between samples. For an optimum sampling scheme, i.e. sampling at the Nyquist rate  $(d_{sx}, d_{sy}) = (1/(2\nu_{x\max}), 1/(2\nu_{y\max}))$ , the interpolating functions have the form [41]:

$$\text{sinc}_{pq}(x, y) = \frac{\sin[2\pi\nu_{x\max}(x - x_p)]\sin[2\pi\nu_{y\max}(y - y_q)]}{[4\pi^2\nu_{x\max}\nu_{y\max}(x - x_p)(y - y_q)]}, \quad (8)$$

Analogous expressions and results can be obtained for the Fourier transform pair formed by  $m(\mathbf{r})$  and its spatial spectrum,  $M(\mathbf{v})$ , related by Eq. (7) after the appropriate substitution of symbols.

### 3. Results

#### 3.1. Artificial zenithal NSB

In order to get some insight about the optimal sampling distance in areas with different artificial light source distributions, we selected four 720x720 km<sup>2</sup> regions of the world and read the predicted values of their artificial zenithal night sky brightness from the NWA floating point dataset [2,3]. Fig 1 shows the corresponding brightness maps, displayed in mag/arcsec<sup>2</sup> logarithmic units, to help visualizing the large dynamic range of the signal. From left to right and top to bottom, the selected regions are centered in Santiago de Compostela, (Galicia), Berlin (Germany), the Joshua Tree National Park (USA), and Swan Hill (Australia). These areas show a variable mix of highly populated cities, rural nuclei, extended oceanic waters and relatively unpopulated lands. As it could be anticipated, their average zenithal night sky brightnesses are widely different, depending on the intensity and spatial distribution of the artificial light sources. The average values of the artificial brightness component in the central 74x74 km<sup>2</sup> part of these regions, separately computed in absolute and relative units, are: Santiago de Compostela (0.29 mcd/m<sup>2</sup>, 21.7 mag/arcsec<sup>2</sup>), Berlin



(0.61 mcd/m<sup>2</sup>, 21.1 mag/arcsec<sup>2</sup>), Joshua Tree Nat. Park (0.17 mcd/m<sup>2</sup>, 23.5 mag/arcsec<sup>2</sup>), and Swan Hill (0.004 mcd/m<sup>2</sup>, 27.6 mag/arcsec<sup>2</sup>).

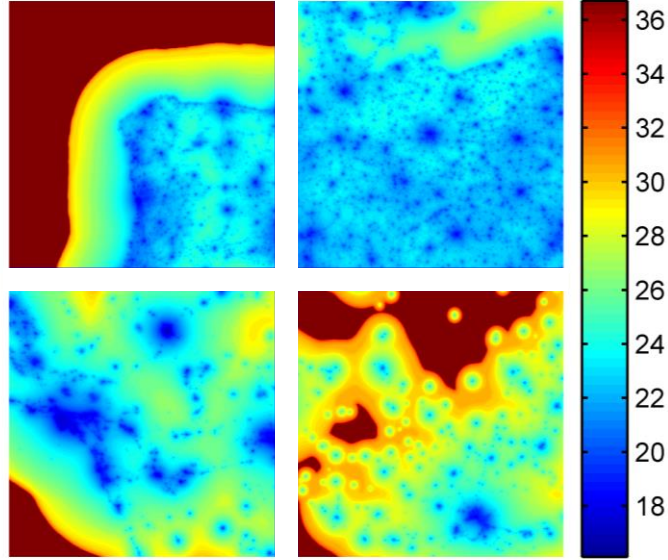


**Figure 1:** Artificial zenithal night sky brightness  $m(\mathbf{r})$  in four regions of the world, according to the NWA estimates [2,3]. Color scale in mag/arcsec<sup>2</sup>. Each region is about 720x720 km<sup>2</sup> wide, and their centers are located at (a) Upper left: Santiago de Compostela, Galicia, Spain (42.8° N, 8.5° W); (b) Upper right: Berlin, Germany (52.5° N, 13.4° E); (c) Lower left: Joshua Tree National Park, California, USA (33.9° N, 115.9° W); (d) Lower right: Swan Hill, Australia (35.5° S, 143.6° E).

Fig. 2 displays the values of  $\sqrt{D_L(\mathbf{d})}$  versus the displacement  $d$ , along the orthogonal latitude and longitude axes, for the central 74x74 km<sup>2</sup> area of the four regions depicted in Fig. 1. Positive values of  $d$  correspond to displacements towards the South (blue), and East (red), respectively. As expected, the absolute brightness differences for a given value of the displacement widely differ from one region to another. Note also that some of the plots tend to saturate for high values of  $d$ . When the displacements are sufficiently larger in comparison with the correlation length of the zenithal sky brightness, the correlation function  $B_L(\mathbf{d})$  tends to the squared

average of the brightness,  $\langle L \rangle^2$ , and hence, according to Eq. (5), the structure function tends to a constant value, equal to  $2(\sigma_L^2 - \langle L \rangle^2)$ .

Fig. 3 displays the expected change in brightness in relative units,  $\sqrt{D_m(\mathbf{d})}$ . The behaviour, in this case, is remarkably similar for all four sites: the slope of  $\sqrt{D_m(\mathbf{d})}$  vs  $d$  for small values of  $d$  is approximately equal to 0.1 mag/arcsec<sup>2</sup> per km in all of them. Of course, the fact that  $\sqrt{D_m(\mathbf{d})}$  has some definite value does not mean that all pixels experience this precise amount of change. Fig. 4 shows the cumulative histogram of the changes in magnitude that a set of observers would record after traveling 1 pixel (0.927 km) southwards, evaluated in the central 74x74 km<sup>2</sup> area of the maps in Fig. 1. Each analyzed region presents a particular histogram signature, with about 69%-87% pixels keeping its absolute brightness differences smaller than  $\pm 0.1$  mag/arcsec<sup>2</sup>.

Figs. 5 and 6 show the spectral power densities  $|\Lambda(\mathbf{v})|^2$  and  $|\mathbf{M}(\mathbf{v})|^2$  of the zenithal night sky brightness maps  $L(\mathbf{r})$  and  $m(\mathbf{r})$ , expressed in absolute and relative units, respectively, taken along two orthogonal axes (longitude and latitude). The maximum spatial frequency contained in these maps is equal to one half the inverse spatial pixel size, that is  $\nu_{y, \max} = 0.54 \text{ km}^{-1}$  along the latitude axis and  $\nu_{x, \max} = 0.54/\cos\phi \text{ km}^{-1}$  along the longitude axis, where  $\phi$  is the latitude. The inspection of these figures does not allow to identify a well-definite spatial cut-off frequency beyond which the spectra become identically zero. This suggests that the Nyquist sampling rate for the zenithal night sky brightness distribution will likely be higher than one sample per km.

Although the spatial spectra in Figs. 5 and 6 do not become strictly zero within the displayed frequency range, their values for spatial frequencies higher than  $\sim 0.25 \text{ km}^{-1}$  are noticeably small. This means that these high-frequency harmonic components contribute in a minor amount to the zenithal NSB, and it suggests that an approximate reconstruction of the zenithal NSB map of the regions under study could be obtained by taking periodically spaced samples separated  $\sim 2$  km. Note that this period is larger than the expected Nyquist sampling rate (the signal is undersampled), so the Nyquist-Shannon theorem does not strictly apply and no exact reconstruction of the brightness between samples is to be expected. However, an approximate reconstruction may be

useful for many practical purposes. As an example of application, Fig. 7 shows the approximate reconstruction of the zenithal sky brightness map from an undersampled signal. Fig. 7(a) shows the central  $74 \times 74 \text{ km}^2$  part of the region around Santiago de Compostela. Fig. 7(b) shows the brightness samples taken every 2 km along the orthogonal latitude/longitude axes. Note that for the purposes of this calculation these samples are assumed to be taken not only in the restricted  $74 \times 74 \text{ km}^2$  area, but across the whole region displayed in Fig. 1 (top left). Fig. 7(c) shows the modulus of the Fourier spectrum of the sampled signal (whole region). This spectrum was multiplied in the spatial frequency space by a two-dimensional super-Gaussian filter  $G(v_x, v_y) = \exp\{-[(v_x/v_c)^8 + (v_y/v_c)^8]\}$ , with  $v_c = 0.25 \text{ km}^{-1}$ , Fig. 7(d), and the result, Fig. 7(e), was transformed back to the spatial domain, Fig. 7(f). The final result closely resembles the actual brightness distribution although, under close inspection, it can be seen that the smallest features become somewhat blurred and some degree of detail is lost, due to undersampling. The root mean squared difference between the original and the reconstructed map in this central area is  $0.0016 \text{ mag/arcsec}^2$ , although individual pixels may show substantially larger differences, in the range  $(-0.33, 0.23) \text{ mag/arcsec}^2$ .

Note that this reconstruction was carried out making use of the samples taken in a region substantially wider than the one shown in Fig. 7(a)-(f). Since the filtering procedure described above is equivalent to interpolating the samples with two-dimensional sinc functions centered at the sampling points, restricting the sampling domain to the small region shown in the figure would give rise to an highly inaccurate reconstruction at the rim of the image, for want of the required contributions from neighbouring points outside this border.

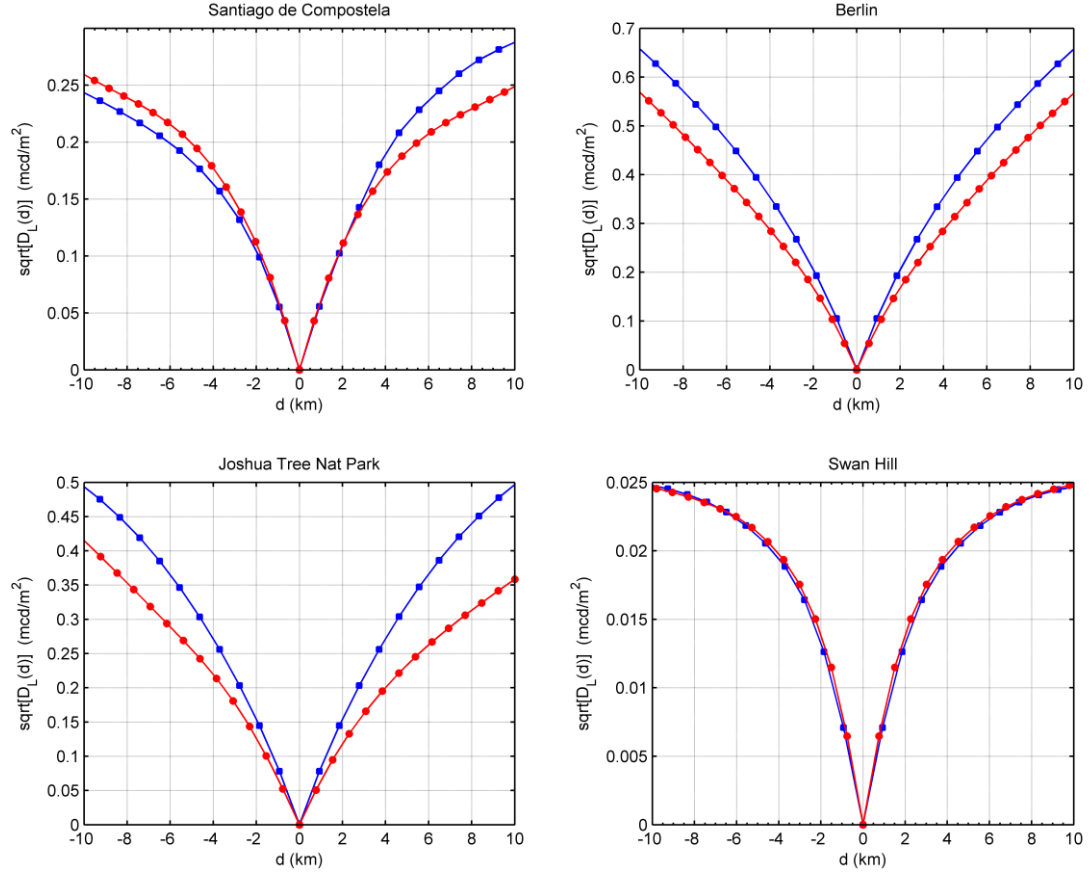


**Figure 2:**  $\sqrt{D_L(d)}$ , the square root of the artificial luminance structure function in  $\text{mcd/m}^2$ , versus the displacement  $d$  in km, evaluated in the central  $74 \times 74 \text{ km}^2$  area of the four regions depicted in Fig. 1. The function is shown for displacements along two orthogonal axes, latitude and longitude. Positive values of  $d$  correspond to displacements towards the South (blue), and East (red), respectively. Note that the expected rms change in absolute brightness for any given displacement strongly depends on the typical brightness levels of each region.

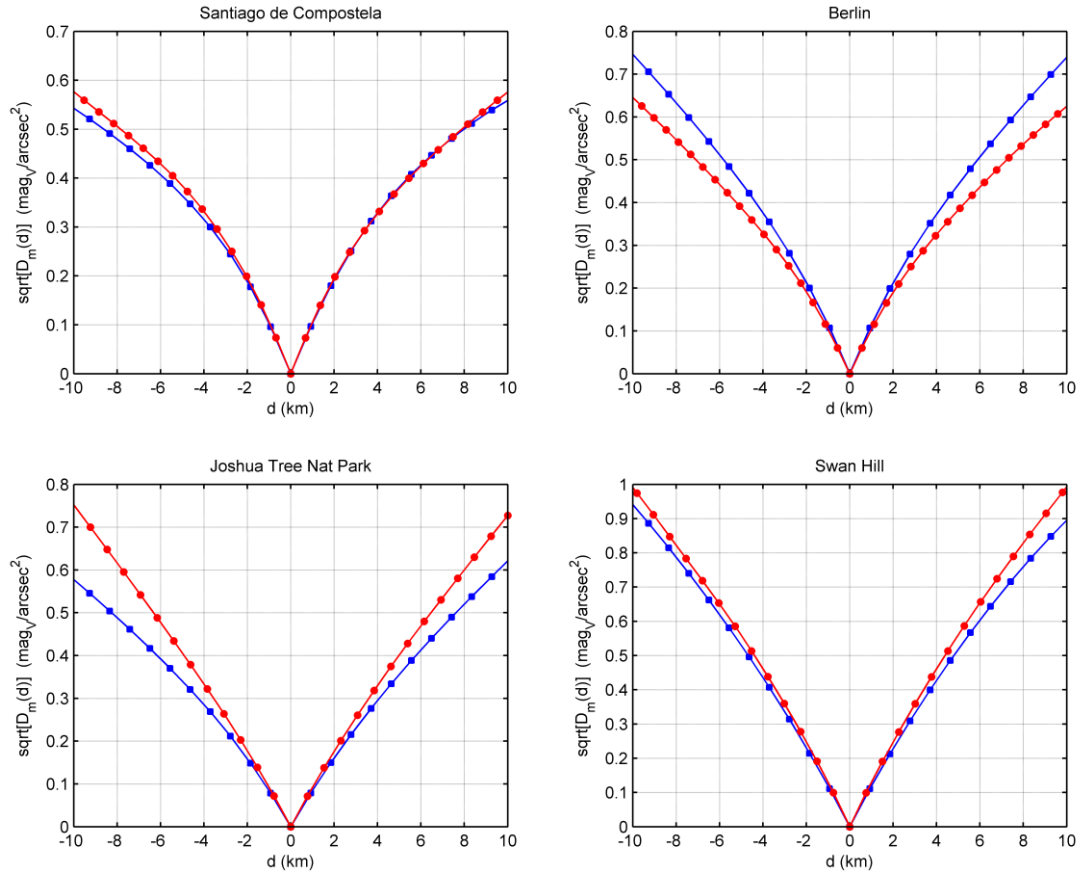


**Figure 3:**  $\sqrt{D_m(d)}$ , the square root of the artificial luminance structure function in  $\text{mag/arcsec}^2$ , versus the displacement  $d$  in km, evaluated in the central  $74 \times 74 \text{ km}^2$  area of the four regions depicted in Fig. 1. Positive values of  $d$  correspond to displacements towards the South (blue), and East (red), respectively. Note that the expected rms change in  $\text{mag/arcsec}^2$  for any displacement is fairly similar in the four areas, independently from the absolute brightness of each one. A rms change of  $\pm 0.1 \text{ mag/arcsec}^2$  is consistently achieved for displacements of order  $\sim 1 \text{ km}$  in all four cases.

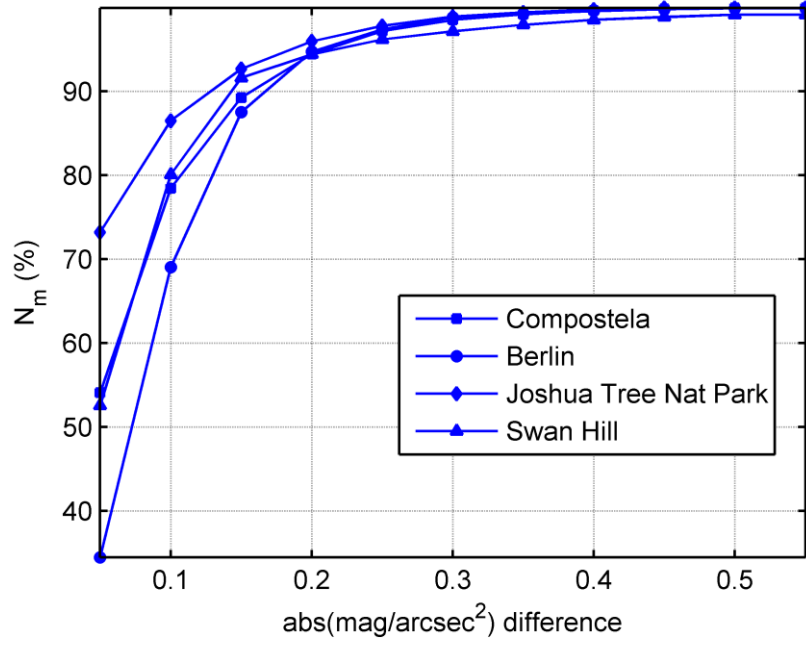


**Figure 4:** Cumulative histogram of the changes in artificial brightness after travelling one pixel southwards (0.927 km), evaluated in the central 74x74 km<sup>2</sup> area of the four regions depicted in Fig. 1.  $N_m$  is the number of pixels (in %) that change their brightness by an absolute amount smaller than the value indicated in the horizontal axis.

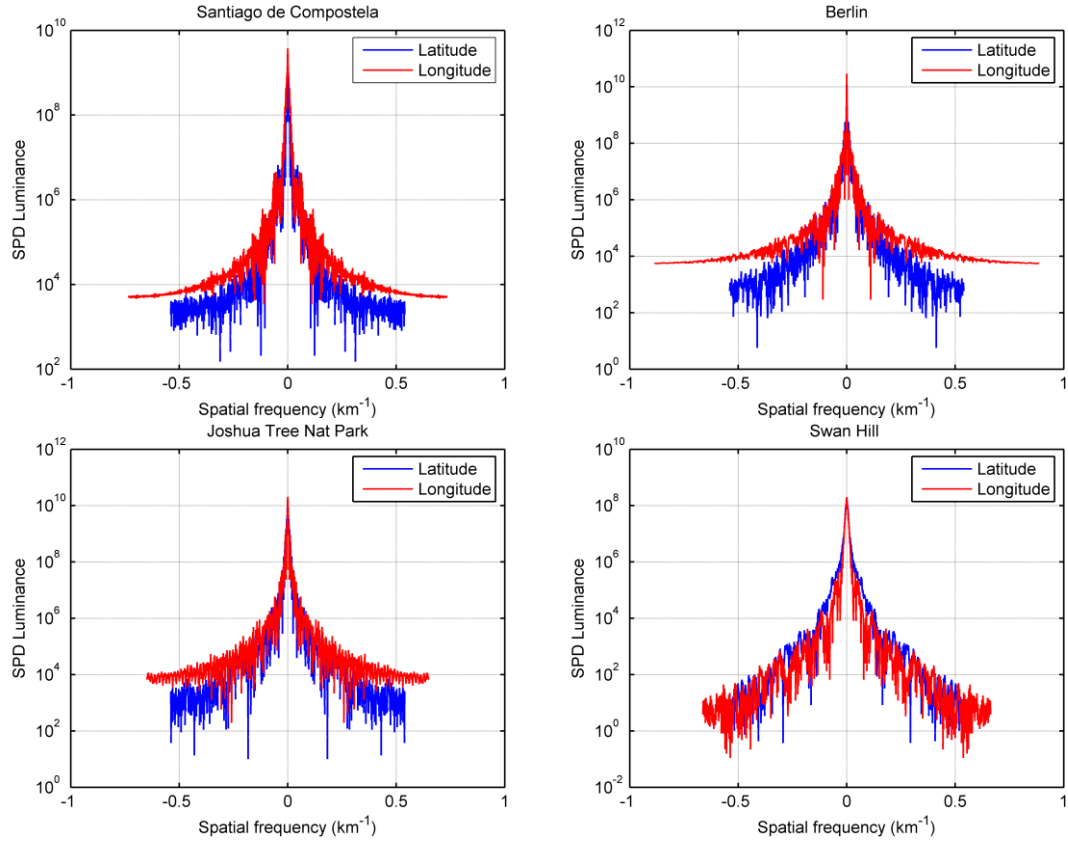


**Figure 5:** Spatial spectral power density  $|\Lambda(\mathbf{v})|^2$  along two orthogonal directions (the local latitude and longitude axes) of the artificial sky brightness distribution  $L(\mathbf{r})$  (mcd/m<sup>2</sup>) in the four regions displayed in Fig. 1.

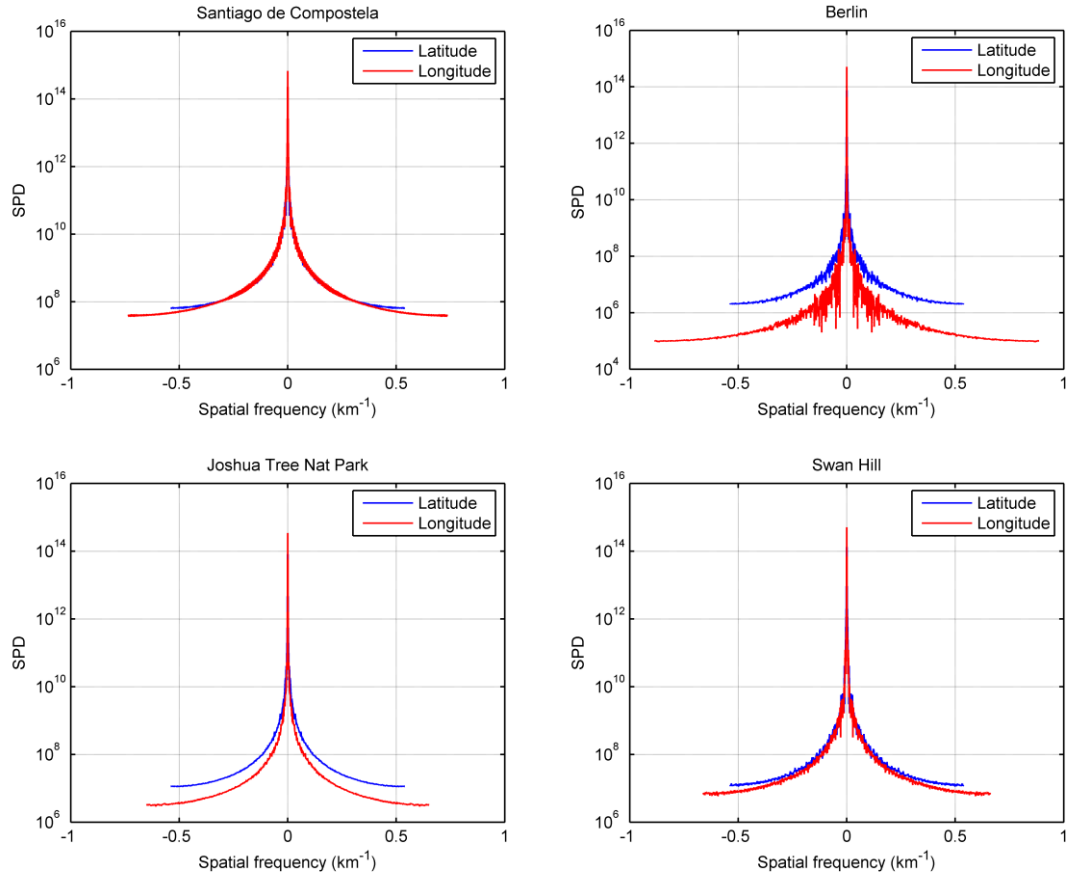


**Figure 6:** Spatial spectral power density  $|M(\mathbf{v})|^2$  along two orthogonal directions (the local latitude and longitude axes) of the artificial sky brightness distribution  $m(\mathbf{r})$  ( $\text{mag}/\text{arcsec}^2$ ) in the four regions displayed in Fig. 1.



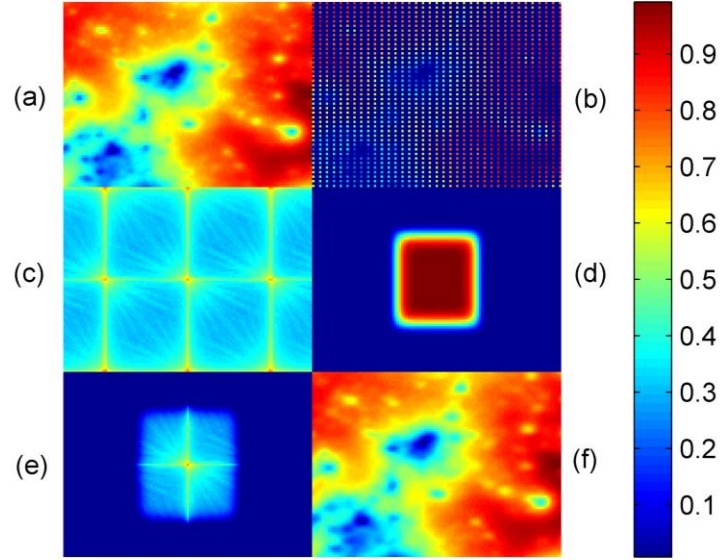


**Figure 7:** Sampling and reconstruction of the continuous artificial zenithal night sky brightness distribution,  $m(\mathbf{r})$ , in the  $720 \times 720 \text{ km}^2$  region centered at Santiago de Compostela ( $42.8^\circ \text{ N}$ ,  $8.5^\circ \text{ W}$ ) using the Nyquist-Shannon theorem. (a) Artificial zenithal night sky brightness  $m(\mathbf{r})$  computed from the luminances of the NWA floating point dataset; (b) Samples of the previous map taken every 2 km in the North-South and East-West directions; (c) Modulus of the two-dimensional spectrum (Fourier transform) of the sampled map; (d) Two-dimensional rectangular low-pass filter with super-Gaussian profile ( $n=8$ ) in the spatial frequency domain; (e) Modulus of the low-pass filtered spectrum of the sampled map; (f) inverse Fourier transform of the low-pass filtered spectrum. The zenithal night sky brightness distribution reconstructed from the discrete set of samples closely resembles the original map. To facilitate the visualization of the middle and high spatial frequency regions of the spectrum, the images (c) and (e) are displayed in a logarithmic scale. In order to discern the individual sampling points in images (a), (b) and (d), only the central  $74 \times 74 \text{ km}^2$  of the whole region are shown. The colorbar is scaled to 1 for the maximum and 0 for the minimum value of each individual image.

### 3.2. Total zenithal NSB

The total zenithal NSB results from adding up to the artificial one the contribution of the natural sources, most notably the celestial objects located above the observer, expressed in energy or light units ( $\text{Wm}^{-2}\text{sr}^{-1}$  or  $\text{cd/m}^2$ ). The total zenithal NSB is a directly measurable physical quantity, and can also be quantitatively estimated by adding to the artificial component the brightness of the natural sky computed by means of suitable models like the one developed by Duriscoe [42]. For the purposes of this work we will assume a constant natural sky contribution of order  $0.174 \text{ mcd/m}^2$ , equivalent to  $22 \text{ mag/arcsec}^2$  in the V band [2]. Figure 8 displays the total zenithal NSB maps of the regions under study, in logarithmic scale.

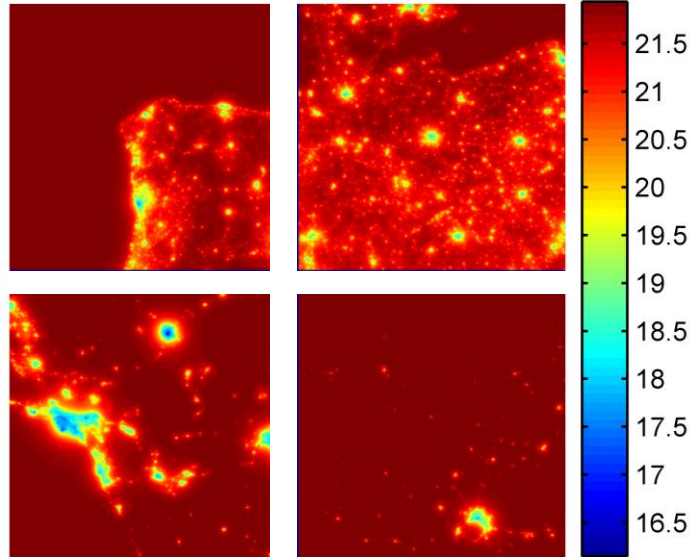


**Figure 8:** Total zenithal night sky brightness  $m(\mathbf{r})$  in the four regions of the world analyzed in this work, according to the NWA estimates [2,3] with an assumed natural sky contribution of  $0.174 \text{ mcd/m}^2$  (equivalent to  $22 \text{ mag/arcsec}^2$ ). Color scale in  $\text{mag/arcsec}^2$ . Each region is about  $720 \times 720 \text{ km}^2$  wide, and their centers are located at (a) Upper left: Santiago de Compostela, Galicia, Spain ( $42.8^\circ \text{ N}$ ,  $8.5^\circ \text{ W}$ ); (b) Upper right: Berlin, Germany ( $52.5^\circ \text{ N}$ ,  $13.4^\circ \text{ E}$ ); (c) Lower left: Joshua Tree National Park, California, USA ( $33.9^\circ \text{ N}$ ,  $115.9^\circ \text{ W}$ ); (d) Lower right: Swan Hill, Australia ( $35.5^\circ \text{ S}$ ,  $143.6^\circ \text{ E}$ ).

Since the natural sky brightness simply adds a constant value in energy or light units to the artificial one, the  $\sqrt{D_L(\mathbf{d})}$  function remains invariant, and the results presented in the previous section directly hold for the total zenithal NSB. Essentially the same happens to the Fourier spectrum  $\Lambda(\mathbf{v})$  of the total brightness, whose only modification is an increase of the DC term, corresponding to the null spatial frequency  $\mathbf{v} = (0,0)$ , which reflects the average value of the zenithal NSB across the geographical region considered. However, if the brightness is expressed in logarithmic mag/arcsec<sup>2</sup> units this invariance does not hold, due to the non linear character of this brightness scale. This can be seen in the behaviour of the total  $\sqrt{D_m(\mathbf{d})}$  function, shown in Fig. 9, as well as in the cumulative histogram corresponding to one pixel displacement southwards, shown in Fig 10. The total magnitude change per km of displacement in direction South is no longer equal in all four zones. As a matter of fact, the existence of a minimum level of zenithal NSB, due to the natural sky contribution, forces the slope of the  $\sqrt{D_m(\mathbf{d})}$  structure function to be smaller. This effect is of minor importance in densely populated regions where the artificial contribution is much higher than the natural one (e.g. Santiago de Compostela or Berlin, which show a behaviour not unlike the one displayed in Fig 3) but clearly affects those areas with low levels of artificial light (see, e.g. Swan Hill).

The slices of the spectral power distribution  $|\mathbf{M}(\mathbf{v})|^2$  of the total zenithal NSB in the four areas under study are displayed in Fig. 11. Again, no clearly cut-off frequency is apparent from the plots, although the fast decay of the SPD enables an approximate reconstruction using an undersampled total zenithal NSB map, as shown in the artificial zenithal NSB case. Fig 12 illustrates this possibility, with samples spaced every 2 km in the Santiago de Compostela region.

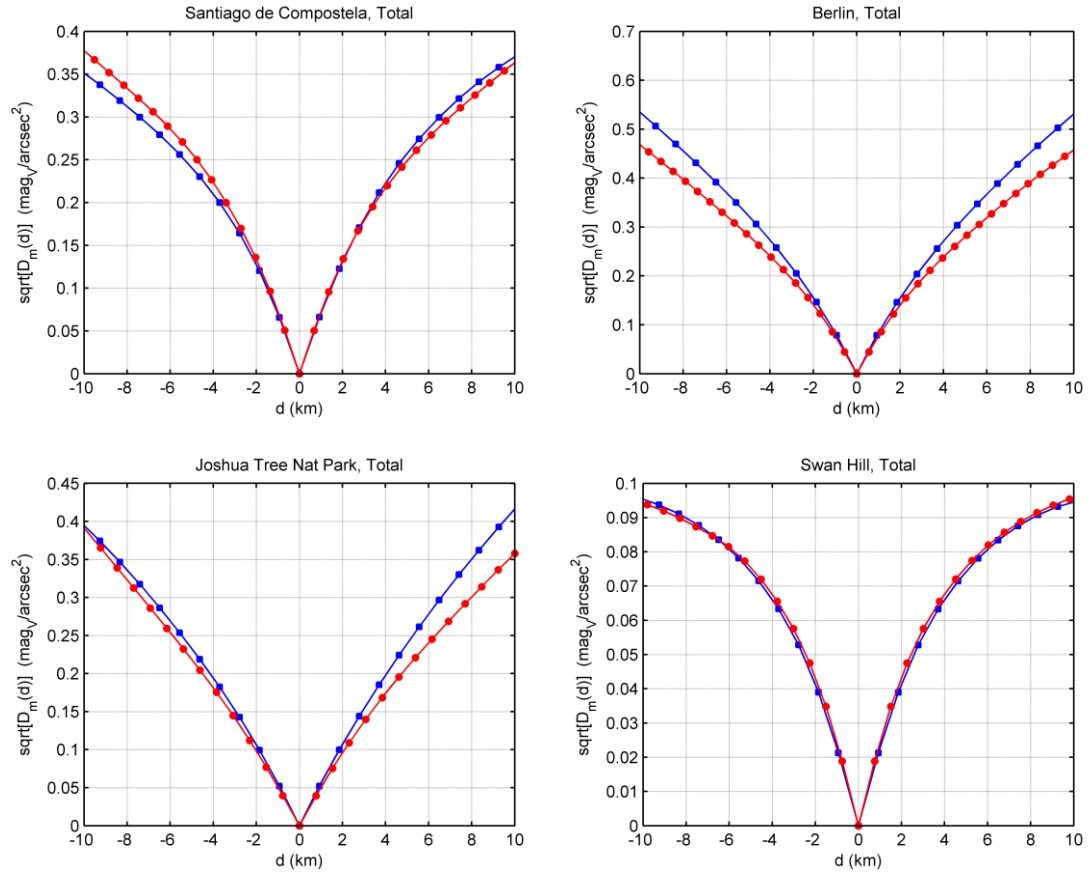


**Figure 9:**  $\sqrt{D_m(d)}$ , the square root of the total luminance structure function in  $\text{mag}/\text{arcsec}^2$ , versus the displacement  $d$  in km, evaluated in the central  $74 \times 74 \text{ km}^2$  area of the four regions depicted in Fig. 1. Positive values of  $d$  correspond to displacements towards the South (blue), and East (red), respectively. Note that the expected rms change in  $\text{mag}/\text{arcsec}^2$  is no longer equal in the four areas.

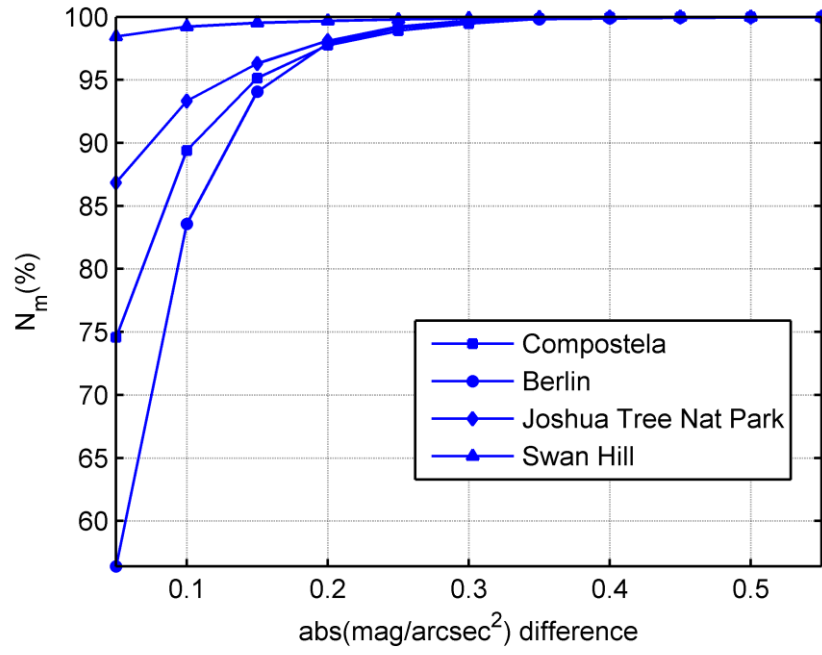


**Figure 10:** Cumulative histogram of the changes in the total brightness after travelling one pixel southwards (0.927 km), evaluated in the central 74x74 km<sup>2</sup> area of the four regions depicted in Fig. 8.  $N_m$  is the number of pixels (in %) that change their brightness by an absolute amount smaller than the value indicated in the horizontal axis.

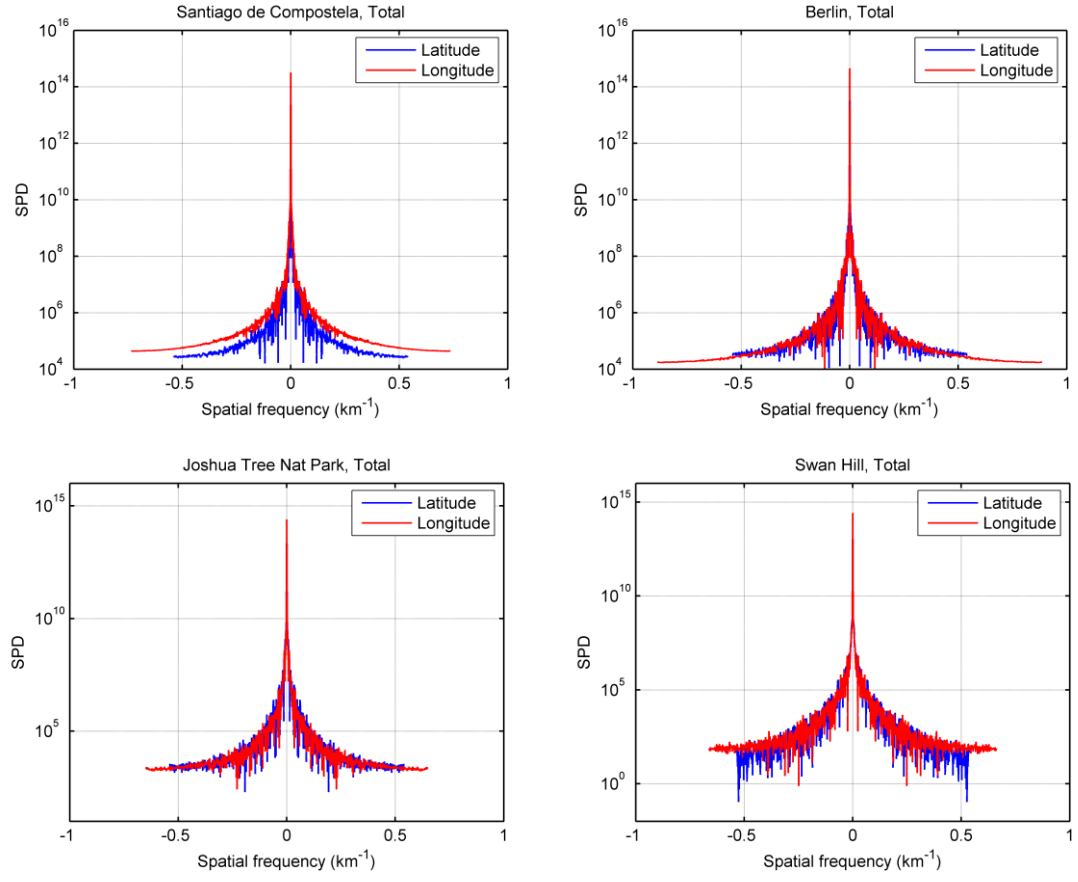


**Figure 11:** Spatial spectral power density  $|\mathbf{M}(\mathbf{v})|^2$  along two orthogonal directions (the local latitude and longitude axes) of the total zenithal sky brightness distribution  $m(\mathbf{r})$  (mag/arcsec<sup>2</sup>) in the four regions displayed in Fig. 8.

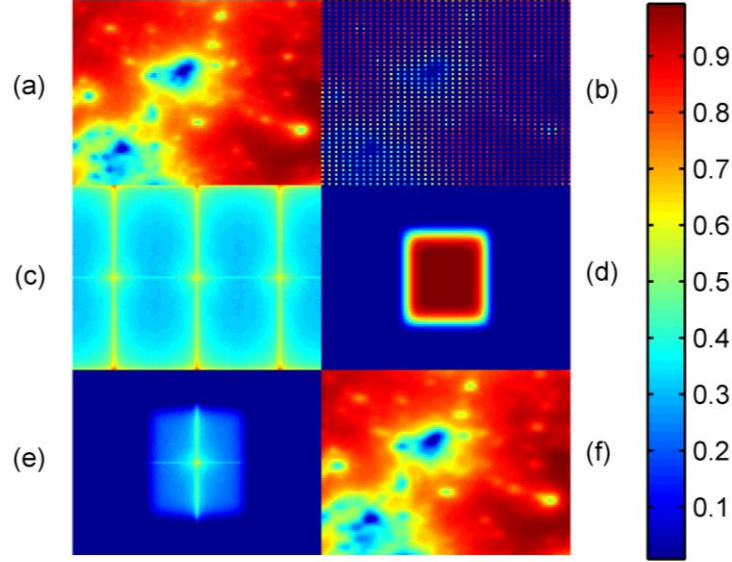


**Figure 12:** Sampling and reconstruction of the continuous total zenithal night sky brightness distribution,  $m(\mathbf{r})$ , in the  $720 \times 720 \text{ km}^2$  region centered at Santiago de Compostela ( $42.8^\circ \text{ N}$ ,  $8.5^\circ \text{ W}$ ) using the Nyquist-Shannon theorem. (a) Total zenithal night sky brightness  $m(\mathbf{r})$  computed from the luminances of the NWA floating point dataset; (b) Samples of the previous map taken every 2 km in the North-South and East-West directions; (c) Modulus of the two-dimensional spectrum (Fourier transform) of the sampled map; (d) Two-dimensional rectangular low-pass filter with super-Gaussian profile ( $n=8$ ) in the spatial frequency domain; (e) Modulus of the low-pass filtered spectrum of the sampled map; (f) inverse Fourier transform of the low-pass filtered spectrum. The zenithal night sky brightness distribution reconstructed from the discrete set of samples closely resembles the original map. To facilitate the visualization of the middle and high spatial frequency regions of the spectrum, the images (c) and (e) are displayed in a logarithmic scale. In order to discern the individual sampling points in images (a), (b) and (d), only the central  $74 \times 74 \text{ km}^2$  of the region are shown. The colorbar is scaled to 1 for the maximum and 0 for the minimum value of each individual image.

#### 4. Discussion

The results presented in this work are intended to be a first approximation to the problem of determining the optimum sampling distance to retrieve the continuous zenithal night sky brightness in a wide territory. Two approaches have been explored. The first one, based on the behaviour of the spatial structure function, provides what can be called a *weak reconstruction criterium*, that is, a sampling distance that guarantees that, in the rms sense, the change in brightness between consecutive sampling points will not surpass a given predefined value. According to this criterium, about one measurement per square kilometer could be sufficient for determining the artificial zenithal night sky brightness at any point of a region to within  $\pm 0.1$  mag/arcsec<sup>2</sup> (in the root-mean-square sense) of its true value in the Johnson-Cousins V band.

The second approach, based on the Nyquist-Shannon spatial sampling theorem, provides a *strong reconstruction criterium*, in the sense that sampling at the Nyquist rate guarantees that an exact reconstruction of the true zenithal night sky brightness distribution can be obtained for all points of the territory. Based on the presently available datasets, the definite value of the required Nyquist rate is still unclear, but will probably lie above one sample per km. An approximate reconstruction of the original brightness can nevertheless be obtained by means of a moderate undersampling: the scenarios described in Section 3 using one sample every two km show the expected performance. Note however that reconstructing a two-dimensional function using the Nyquist-Shannon approach within a finite domain often requires acquiring a huge number of samples in the region surrounding it, which can be impractical in many situations.

Other reconstruction schemes, and in particular least-squares fits of different families of orthogonal polynomials whose domain of definition be coincident with the region of interest, could prove to be more useful for retrieving the continuous zenithal brightness maps from finite sets of samples. These possibilities have not been addressed in this work, and deserve further research.



As a final remark, the methods here described can be equally applied to the reconstruction of the night sky brightness in any arbitrary direction of the celestial hemisphere (not just the zenithal one), from a discrete set of samples taken in different points of the territory. The optimum sampling distance does not have to be the same for all hemispheric directions, and the minimum of its values should be taken as a reference for carrying out theoretical calculations or planning observational field campaigns. As it has previously been shown, the all-sky brightness distribution at any given site can be reconstructed from a finite number of samples taken in different directions of the celestial hemisphere [43-45]. An optimum sampling scheme, combining directional (across the upper hemisphere in the observer's reference frame) and spatial (across the territory) measurements may open the way to the reconstruction of the all-sky night brightness distributions at any place of the region of interest.

## 5. Conclusions

Two different tools were used to determine the optimum sampling distance in order to retrieve, with sufficient accuracy, the continuous zenithal night sky brightness map across a wide territory: the luminance structure function and the Nyquist-Shannon spatial sampling theorem. The analysis of several regions of the world suggests that, as a rule of thumb, about one measurement per square kilometer could be sufficient for determining the artificial zenithal night sky brightness at any point of a region to within  $\pm 0.1 \text{ mag/arcsec}^2$  (in the root-mean-square sense) of its true value in the Johnson-Cousins V band. The exact reconstruction of the zenithal night sky brightness map from samples taken at the Nyquist rate seems to be considerably more demanding.

## Acknowledgments

This work was developed within the framework of the Spanish Network for Light Pollution Studies (AYA2015-71542-REDT). The availability of the floating point dataset of the *New world atlas of artificial night sky brightness* is gratefully acknowledged.

## References

1. Cinzano, P., Falchi, F., Elvidge, C. (2001). The first world atlas of the artificial night sky brightness. *Mon. Not. R. Astron. Soc.*, 328, 689–707.
2. Falchi, F., Cinzano, P., Duriscoe, D., Kyba, C.C.M., Elvidge, C.D., Baugh, K., Portnov, B.A., Rybnikova, N.A., Furgoni, R. (2016). The new world atlas of artificial night sky brightness. *Sci. Adv.* 2, e1600377. (doi: 10.1126/sciadv.1600377)
3. Falchi, F., Cinzano, P., Duriscoe, D., Kyba, C.C.M., Elvidge, C.D., Baugh, K., Portnov, B., Rybnikova, N.A., Furgoni, R. (2016). Supplement to: The New World Atlas of Artificial Night Sky Brightness. GFZ Data Services. <http://doi.org/10.5880/GFZ.1.4.2016.001>
4. Kyba, C.C.M. et al. (2015) Worldwide variations in artificial skyglow. *Sci. Rep.* 5, 8409. doi:10.1038/srep08409.
5. Bará, S. (2016). Anthropogenic disruption of the night sky darkness in urban and rural areas, *Royal Society Open Science* 3: 160541. doi: 10.1098/rsos.160541. Published 19 October 2016
6. Garstang, R.H. (1986). Model for artificial night-sky illumination. *Publ. Astron. Soc. Pac.* 98, 364-375.
7. Cinzano, P., Falchi, F., Elvidge, C.D. (2001) Naked-eye star visibility and limiting magnitude mapped from DMSP-OLS satellite data. *Mon. Not. R. Astron. Soc.* 323, 34–46.
8. Cinzano, P., Elvidge, C.D. (2004). Night sky brightness at sites from DMSP-OLS satellite measurements. *Mon. Not. R. Astron. Soc.* 353, 1107–1116 doi:10.1111/j.1365-2966.2004.08132.x
9. Kocifaj, M. (2007). Light-pollution model for cloudy and cloudless night skies with ground-based light sources. *Applied Optics* 46, 3013-3022
10. Cinzano, P., Falchi, F. (2012). The propagation of light pollution in the atmosphere. *Mon. Not. R. Astron. Soc.* 427, 3337–3357. doi:10.1111/j.1365-2966.2012.21884.x

11. Kyba, C.C.M., Ruhtz, T., Fischer, J., and Hölker, F. (2012). Red is the new black: how the colour of urban skyglow varies with cloud cover. *Mon. Not. R. Astron. Soc.* 425, 701–708. doi:10.1111/j.1365-2966.2012.21559.x
12. Aubé, M. (2015). Physical behaviour of anthropogenic light propagation into the nocturnal environment. *Phil. Trans. R. Soc. B* 370:20140117. doi: 10.1098/rstb.2014.0117
13. Kocifaj, M. (2016). A review of the theoretical and numerical approaches to modeling skyglow: Iterative approach to RTE, MSOS, and two-stream approximation. *Journal of Quantitative Spectroscopy & Radiative Transfer* 181, 2–10.
14. Solano Lamphar, H.A., and Kocifaj, M. (2016). Urban night-sky luminance due to different cloud types: A numerical experiment *Lighting Res. Technol.*, 48, 1017–1033. doi: 10.1177/1477153515597732
15. Ribas, S.J., Torra, J., Figueras, F., Paricio, S., Canal-Domingo, R. (2016). How Clouds are Amplifying (or not) the Effects of ALAN. *International Journal of Sustainable Lighting*, 35, 32-39. doi: 10.22644/ijsl.2016.35.1.032
16. Aubé, M., Kocifaj, M., Zamorano, J., Solano Lamphar, H.A., Sánchez de Miguel, A. (2016) The spectral amplification effect of clouds to the night sky radiance in Madrid. *Journal of Quantitative Spectroscopy & Radiative Transfer* 181, 11–23.
17. Longcore, T., Rich, C. (2004). Ecological light pollution. *Frontiers in Ecology and the Environment* 2, 191-198.
18. Rich, C., Longcore, T., editors. (2006). *Ecological consequences of artificial night lighting*. Washington, D.C.: Island Press.
19. Navara, K.J., Nelson, R.J. (2007). The dark side of light at night: physiological, epidemiological, and ecological consequences. *J. Pineal Res.* 43, 215-224.
20. Hölker, F., Wolter, C., Perkin, E.K., Tockner, K. (2010). Light pollution as a biodiversity threat. *Trends in Ecology and Evolution* 25, 681-682.
21. Gaston, K.J., Bennie, J., Davies, T.W., Hopkins, J. (2013). The ecological impacts of nighttime light pollution: a mechanistic appraisal. *Biological Reviews* 88, 912–927.

22. Gaston, K.J., Duffy, J.P., Gaston, S., Bennie, J., Davies, T.W. (2014). Human alteration of natural light cycles: causes and ecological consequences. *Oecologia* 176, 917–931.
23. Hölker, F., Moss, T., Griefahn, B., Kloas, W., Voigt, C.C., Henckel, D., Hänel, A., Kappeler, P.M., Völker, S., Schwöpe, A., Franke, S., Uhrlandt, D., Fischer, J., Klenke, R., Wolter, C., Tockner, K. (2010). The dark side of light: a transdisciplinary research agenda for light pollution policy. *Ecology and Society* 1 (4): 13. ([www.ecologyandsociety.org/vol15/iss4/art13/](http://www.ecologyandsociety.org/vol15/iss4/art13/))
24. Duriscoe, D.M., Luginbuhl, C.B., Moore, C.A. (2007). Measuring Night-Sky Brightness with a Wide-Field CCD Camera. *Publications of the Astronomical Society of the Pacific*, 119(852), 192-213.
25. Rabaza, O., Galadí-Enríquez, D., Espín Estrella, A., Aznar Dols, F. (2010). All-Sky brightness monitoring of light pollution with astronomical methods. *Journal of Environmental Management*, 91, 1278e1287.
26. Falchi, F. (2011). Campaign of sky brightness and extinction measurements using a portable CCD camera. *Mon. Not. R. Astron. Soc.*, 412, 33–48. doi: 10.1111/j.1365-2966.2010.17845.x
27. Aceituno, J., Sánchez, S. F., Aceituno, F. J., Galadí-Enríquez, D., Negro, J. J. , Soriguer, R. C., and Sanchez-Gomez, G. (2011). An all-sky transmission monitor: ASTMON. *Publ. Astron. Soc. Pac.*, 123, 1076–1086.
28. Kolláth, Z. (2010). Measuring and modelling light pollution at the Zselic Starry Sky Park. *Journal of Physics: Conference Series*, 218, 012001. doi: 10.1088/1742-6596/218/1/012001
29. Jechow, A., Kolláth, Z., Lerner, A., Hölker, F., Hänel, A., Shashar, N., Kyba, C.C.M. (2017). Measuring Light Pollution with Fisheye Lens Imagery from A Moving Boat, A Proof of Concept. *arXiv:1703.08484v1 [q-bio.OT]* 22 Mar 2017
30. Duriscoe D. (2016). Photometric indicators of visual night sky quality derived from all-sky brightness maps. *Journal of Quantitative Spectroscopy & Radiative Transfer*, 181, 33–45. doi: 10.1016/j.jqsrt.2016.02.022
31. Pun, C.S.J., So, C.W. (2012). Night-sky brightness monitoring in Hong Kong: A city-wide light pollution assessment. *Environ Monit Assess*, 184, 2537–2557. doi: 10.1007/s10661-011-2136-1

32. Espey, B., McCauley, J. (2014). Initial Irish light pollution measurements and a new Sky Quality Meter-based data logger. *Lighting Res. Technol.* 46, 67–77.
33. Puschig, J., Schwöpe, A., Posch, T., Schwarz, R. (2014). The night sky brightness at Potsdam-Babelsberg including overcast and moonlit conditions. *Journal of Quantitative Spectroscopy & Radiative Transfer*, 139, 76–81.
34. Puschig, J., Posch, T., Uttenthaler, S. (2014). Night sky photometry and spectroscopy performed at the Vienna University Observatory. *Journal of Quantitative Spectroscopy & Radiative Transfer*, 139, 64–75.
35. den Outer, P., Lolkema, D., Haaijma, M., van der Hoff, R., Spoelstra, H., Schmidt, W. (2015). Stability of the Nine Sky Quality Meters in the Dutch Night Sky Brightness Monitoring Network. *Sensors*, 15, 9466-9480. doi: 10.3390/s150409466
36. Zamorano, J., Sánchez de Miguel, A., Ocaña, F., Pila-Diez, B., Gómez Castaño, J., Pascual, S., Tapia, C., Gallego, J., Fernandez, A., Nievas, M. (2016). Testing sky brightness models against radial dependency: a dense two dimensional survey around the city of Madrid, Spain. *Journal of Quantitative Spectroscopy & Radiative Transfer*, 181, 52–66. doi: 10.1016/j.jqsrt.2016.02.029
37. Bessell, M.S. (1979) UBVRI photometry II: The Cousins VRI system, its temperature and absolute flux calibration, and relevance for two-dimensional photometry. *Publ. Astron. Soc. Pac.* 91, 589–607.
38. CIE, Commission Internationale de l'Éclairage. (1990) *CIE 1988 2° Spectral Luminous Efficiency Function for Photopic Vision*. Vienna: Bureau Central de la CIE.
39. Sánchez de Miguel, A., Aubé, M., Zamorano, J., Kocifaj, M., Roby, J., Tapia, C. (2017). Sky Quality Meter measurements in a colour changing world. *Mon Not R Astron Soc*, 467(3), 2966-2979. doi: /10.1093/mnras/stx145
40. Papoulis, A. (1981). *Systems and transforms with applications in optics*. R.E. Krieger, Florida. pp.119-128.
41. Goodman, J.W. (1996). *Introduction to Fourier Optics*, 2nd. ed. McGraw-Hill, New York. pp. 22-26.

42. Duriscoe D.M. (2013). Measuring Anthropogenic Sky Glow Using a Natural Sky Brightness Model. Publications of the Astronomical Society of the Pacific, 125(933), 1370-1382. <http://www.jstor.org/stable/10.1086/673888>
43. Bará, S., Nievas, M., Sánchez de Miguel, A., and Zamorano, J. (2014). Zernike analysis of all-sky night brightness maps. Applied Optics, 53(12), 2677-2686. doi: 10.1364/AO.53.002677
44. Bará, S., Tilve, V., Nievas, M., Sánchez de Miguel, A., and Zamorano, J. (2015). Zernike power spectra of clear and cloudy light-polluted urban night skies. Applied Optics, 54(13), 4120-4129. doi: 10.1364/AO.54.004120
45. Bará, S., Ribas, S., and Kocifaj, M. (2015). Modal evaluation of the anthropogenic night sky brightness at arbitrary distances from a light source. Journal of Optics (IOP) 17, 105607. doi:10.1088/2040-8978/17/10/105607